Structural and dynamic phase transitions of NaNbO3 from first-principles calculations

Safari, Amisi; Lambin, Philippe; Ghosez, Philippe

Published in:
Physical Review Materials

DOI:
10.1103/PhysRevMaterials.7.024408

Publication date:
2023

Document Version
Early version, also known as pre-print

begindocument/before

Structural and dynamic phase transitions of $NaNbO_3$ from first-principles calculations

Safari Amisi[1,2], Philippe Lambin[1,2], and Philippe Ghosez[3]

[1] *Laboratoire de Physique des Solides et des Interfaces,*

Institut Supérieur Pédagogique de Bukavu, Democratic Republic of the Congo

[2] *Laboratoire de Physique des Solides,*

Université de Namur, Belgium and

[3] *Physique Théorique des Matériaux,*

Université de Liège, B-4000 Sart Tilman, Belgium

Abstract

The crystal structures and phase transitions of $NaNbO_3$ are analyzed with density fonctional theory through GGA-PBEsol and LDA approximations. The phonon dispersion curves from the high-symmetry cubic perovskite phase are reported to have many unstable branches, predisposing it to several combinations of phase transitions to various distorted structures. The lattice parameters are optimized and the results are compared with existing experimental and theortical data. The indirect band gap is observed for the cubic phase. Many phases, observed and unobserved experimentally, are analyzed mode by mode. Our work reveals that, more than in $PbZrO_3$, given their all important potential wells, none of the individual modes condensed deletes all other but it is their coupling which plays a key role in the condensation of the ground state sodium niobate. This work points out the importance of instabilities at R and M points of the first Brillouin zone and along the line T (connecting the M and R points) to stabilize the low energy phases. Within GGA-PBEsol approximation, the ground state is rhombohedral FE/AFD $R3c$, while in LDA it is rather the orthorhombic FE/AFD $Pmc2_1$ structure that stabilizes the lowest energy in this compound. In both calculations we find small energy difference between the three lowest energy phases $Pmc2_1$ (FE/AFD[110]), $Pbcm$ (AFE/AFD), and $R3c$ (FE/AFD[111]), which is a key characteristic of antiferroelectricity. The GGA-PBEsol approach provides more sensible results than the LDA approximation.

I. INTRODUCTION

Antiferroelectric (AFE) materials are promising candidates for a wide range of electronic applications, such as high-energy storage capacitors[1], electrocaloric refrigerators[2], and non-volatile random access memories[3]. Among them, $NaNbO_3$ (NNO), known for its complex structures and phase transitions[4,5], is one of the very few lead-free antiferroelectric oxides. This material has attracted considerable interest because it is a typical nontoxic and highly-stable semiconductor which has applications in photocatalysis[6] and potentially also in piezoelectric nano-devices[7]. Indeed, NNO receives a growing interest in environmental protection, providing a matrix phase for various lead-free piezoelectric materials, such as (K, Na, Li)(Nb, Ta, Sb)O_3[8] and (Na, K)NbO_3[9], which could replace the set of lead-based perovskites.

ABO_3 perovskites typically cristallise at high temperature in an aristotype cubic $Pm\bar{3}m$ structure but then lower their symmetry on cooling by rotating or distorting the BO_6 octahedra and translating the A site or B site cations. The structures obtained by simple rotations of the BO_6 octahedra around the axes of the aristotype cubic structure were first classified by Glazer[10], followed by a number of theoretical studies of the possible tilt structures and phase transitions[11–13]. It is known today that understanding the crystal structures, characterized by structural phase transitions, of the perovskites is crucial to understand the origin of their performance, and accelerate the search for new materials. The computational first-principles approach has became an extremely valuable tool to identify competing structural instabilities in perovskites, and this is even more crucial for a structurally complex material such as NNO.

The richness of the phonon curves in the cubic phase and the complex sequence of phase transitions of NNO are the subject of several studies both experimental and theoretical. Discovered in 1949 by Matthias[14], NNO certainly represents the most structurally complex "simple" perovskite known so far. A set of "seven phases of sodium niobate" were first summarized by Megaw[15] : N (FE/AFD-$R3c$, below -100°C), P (AFE/AFD-$Pbcm$, from -100 to 360°C, room temperature), R (AFE/AFD-$Pnmm$, 360 $\rightarrow$ 480°C), S (PE/AFD-$Pnmm$, 480 $\rightarrow$ 520°C), T_1 (PE/AFD-$Cmcm$, 520 $\rightarrow$ 575°C), T_2 (PE/AFD-$P4/mbm$, de 575 $\rightarrow$ 640°C), and U (PE-$Pm\bar{3}m$, beyond 640°C); PE, AFD, AFE, and FE are abbreviations for paraelectric, antiferrodistortive, antiferroelectric, and ferroelectric, respectively. Since

then, several additional phases have been put forward. It is the case of the Q (FE/AFD-$Pmc2_1$) phase, visible as a phase coexisting in certain temperature ranges with the N and P phases[16–20].

In spite of the importance of phonons in the physics of ferroelectrics, there are rare studies in the literature on the phonon-dispersion relation of NNO from first-principles[21]. The present first-principles study aims to improve our understanding of the crystal structures, phase transitions and phase stability of sodium niobate.

In this paper we quantify the delicate competitions between instabilities in NNO, we systematicaly analyse the phase transition mecanism and discuss how it affects the volume and atomics displacements. We confirm the presence of mixtures of the $Pmc2_1$ (FE[110]/AFD), $Pbcm$ (AFE/AFD), and $R3c$ (FE[111]/AFD) polymorphs. Compared to experimental observations, our GGA-PBEsol approach provides more sensible results than LDA approximations. However, let us emphasize the fact that the R AFE/AFD-$Pnmm$ and S PE/AFD-$Pnmm$, with cells dimension $\sqrt{2}\times\sqrt{2}\times 12$ (24 formula units) and $\sqrt{2}\times 6\times\sqrt{2}$ (12 formula units), respectively, are more complex to build and to characterize from ab initio simulations[22].

The remainder of this paper is organised as follows. In the following Section II, we summarize the technical details of our calculations. The description of the cubic perovskite phase, including the lattice constant, the Born effective charges, and the phonon dispersion curves are reported in Section III. Section IV discusses the FE, AFD and antipolar electric (APE) instabilities condensed one by one and the relative low energy structure for each them. In the Section V, we investigate the ground state in NNO and the energy proximity between FE and AFE phases. We finish with a conclusion.

II. COMPUTATIONAL DETAILS

First-principles calculations were carried out using the ABINIT density functional theory (DFT) package[23–25], a planewave pseudopotential approach using the optimized norm-conserving pseudopotentials (ONCVPSP)[26–28], available on pseudo-dojo server[29]. All of the present ab initio calculations were performed using our optimized theoretical lattice constants. The Perdew-Burke-Ernzerhof functional revised for solids (GGA−PBEsol)[30] was mainly employed, and, for comparison, some results have been checked at the local density

approximation (LDA) level using Teter's extended norm conserving pseudopotentials[31]. The valence states for the computations are $2s^2 2p^6 3s^1$ for Na, $4s^2 4p^6 4d^4 5s^1$ for Nb and $2s^2 2p^4$ for O. Convergence was acheaved for an energy cutoff of 45 hartrees for the plane-wave expansion (for both types of pseudopotentials) and a 8×8×8 grid of k-points for the Brillouin zone sampling of the single perovskite 5-atom cell. When condensing the AFD instabilities, either we considered a 20-atom supercell corresponding to $\sqrt{2}a_0$, $\sqrt{2}a_0$, $2a_0$, with a sampling of 6×6×4 k-points or, for the $Cmcm$, $Pmmn$, $R\bar{3}c$ and $R3c$ phases, a 40-atom supercell corresponding to $2a_0$, $2a_0$, $2a_0$ with a sampling of 4×4×4 k-points. The antipolar electric (APE) $Cmc2_1$, AFD $a^-a^-b^+/a^-a^-b^-$, and AFE/AFD $Pbcm$ structures were relaxed in 40 atoms supercell corresponding to $\sqrt{2}a_0$, $\sqrt{2}a_0$, $4a_0$ and a sampling of 6×6×2 k-points. We explicitly checked that the relative energy of the different phases is well converged and independent of the choice of the supercell. Structural relaxations were performed until the forces and stresses were smaller than 10^{-7} hartrees/bohr and 10^{-7} hartrees/bohr^3 respectively. The phonon frequencies, with a sampling of 8×8×8 and 6×6×2 k-points, Born effective charges, and electronic dielectric tensor, with a sampling of 8×8×8 k-points, were calculated according to density functional perturbation theory (DFPT)[32]. For the polarization, we used the Berry phase calculation[33]. The space group symmetry were checked by FINDSYM program[34]. To analyse the group theory and relative contributions of different phonon modes to the distortions, we employed ISOTROPY and AMPLIMODES codes of Crystallographic Bilbao server[35–37].

III. HIGH-SYMMETRY CUBIC STRUCTURE

First, we report the properties of the highly-symmetric cubic perovskite structure of NNO. In this cubic phase, the atomic positions are fixed by symmetry and the only structural parameter to be relaxed is the lattice constant a_0. Our results are reported in Table I compared to $NaTaO_3$ (AFD), $KNbO_3$ (FE) and $KTaO_3$ (PE), and other theoretical and experimental values. We report also the Born effective charges (Z^*) and the optical dielectric constant (ϵ^∞). In the cubic structure, Z^* of A (A = Na; K) and B (B = Nb; Ta) atoms are isotropic while, for O, two distinct values have to be considered depending if the O atom is displaced along the B−O chain ($O_\parallel$) or perpendicularly to it ($O_\perp$).

Our NNO relaxed lattice constant (a_0 = 3.9427 Å) is in agreement with that reported

TABLE I. Lattice parameter (Å), Born effective charges ($|e|$), optical dielectric constant GAP (eV) and the calculated Goldschmidt tolerance factor t of cubic $NaNbO_3$ at relaxed volume compared to $NaTaO_3$ (AFD), $KNbO_3$ (FE) and $KTaO_3$ (PE), and other theoretical values. ^{a}: GGA−PBEsol, ^{b}: LDA. The nominal charge are $+1|e|$ for Na and K ions, $+5|e|$ for Nb and Ta ions, and $-2|e|$ for O ion. The $NaNbO_3$ experimental lattice parameter and GAP are respectively 3.945 Å and 3.4 eV[38].

	$NaNbO_3$			$NaTaO_3$	$KNbO_3$	$KTaO_3$
	Present	LDA	US-PP[39]	Present	Present	Present
a_0	3.9427^a		4.1822	3.9366^a	3.9847^a	3.9772^a
	3.9134^b	3.92[40]				
Z^*_A	1.13	1.13[41]	1.102	1.14	1.14	1.15
Z^*_B	9.48	9.11	9.718	8.56	9.61	8.68
$Z^*_{O_\parallel}$	−7.28	−7.01	−6.28	−6.50	−7.28	−6.49
$Z^*_{O_\perp}$	−1.67	−1.61	−2.27	−1.60	−1.73	−1.67
ϵ^∞	6.12	4.96		5.12	6.42	5.39
GAP	1.65	1.6[40]		2.32	1.53	2.16
t	0.94			0.92	1.04	1.02

experimentally ($a_0 = 3.945$ Å) and with other theoretical results (Tab. I). Let us nevertheless point out the discrepansy with the values found by Prosandeev[39] who used the ultrasoft atomic potentials (US-PP).

The Born effective charges of B (B = Nb; Ta) and $O_\parallel$ are strongly anomalous, and these values are known to be a common feature of ABO_3 compounds. They are related to dynamical transfer of charge between the B d and O $2p$ orbitals[42]. $Z^*_{(Na/K)}$ and $Z^*_{O_\perp}$ are also anomalous but to a much lower extent. We notice the tendency of the Born effective charges to be larger in niobates ($ANbO_3$) than in tantalates ($ATaO_3$). In the same way, the calculated optical dielectric constant of $ANbO_3$ (6.12 and 6.42) is greater than for $ATaO_3$ (5.12 and 5.39).

Our calculations describe NNO as an insulator with an indirect bandgap of 1.65 eV between R and Γ points, as well as for $NaTaO_3$ (2.32 eV), $KNbO_3$ (1.53 eV), and $KTaO_3$ (2.16 eV). This result is in agreement with the previous theoretical value 1.6 eV[40]. Compared with the experimental band gap 3.4 eV of NNO[43], the calculated indirect band gap is much

smaller. This discrepancy is due to the use of GGA, or LDA, which typically underestimates, by about 30 to 40%, the experimental band gap in semiconductors and insulators[44] but correctly reproduces their insulating nature. Note, however, that the hybrid functionals give a bandgap value in much better agreement with the experiment, as demonstrated by Bilc *et al.* on the $BaTiO_3$ (Exp.: 3.2; B3LYP: 3.7, B1-WC: 3.4)[45].

Even if the ground state of a system can be more complex, the calculation of phonon dispersion curves in the high-symmetry phase offers a global view of the instabilities that can progressively condense, to reveal the possible intermediate phases and the ground state. The Goldschmidt tolerance factors of NNO ($t < 0.98$) and $NaTaO_3$ materials are close, and dispose them to stabilize in an orthorhombic AFD phase. In Figure 1 we report the phonon dispersion curves of NNO and $NaTaO_3$ in cubic 5-atom cell. The $R-\Gamma$, $\Gamma-X$, $X-M$ and $M-\Gamma$ lines are along the [111], [100], [010] and [110] directions, respectively. Negative values of ω (cm^{-1}) in the graphs correspond to imaginary phonon frequencies and are related to unstable modes, which determine the nature of eventual phase transitions. By condensing these unstable modes, it is theoretically possible to find the intermediate and the stable phases of a compound. The character of these modes also has significant implications on system properties. Frequencies and types of ferroic unstable modes are summarized in Table II.

Our cubic NNO phonon curves are in agreement with those calculated by Machado *et al.*[21] but different to those calculated by Prosandeev[39], in wich the R unstable mode is the most significant. As can be seen from Figure 1, the ferroelectric instability in NNO, contrary to that in $NaTaO_3$, is not restricted to the Γ point, but extends to $\Gamma-X-M$ plane, and the AFD unstable branches extend from M to R in both structures. In NNO there are additional unstable branches.

In $NaTaO_3$, instabilities are dominated by AFD R_4^+ and M_3^+ modes, but in NNO, similar to what is observed for the $PbZrO_3$ (PZO)[46], the polar FE (Γ_4^-) and antipolar (Δ_5, X_5^-, M_3^- and T_4) instabilities are also significant. For the instability at Γ point, the eigendisplacement in NTA is significantly dominated by the movement in opposite directions of Na and O atoms, with a very small displacement of the Ta atom because of its heaviness (almost six times the mass of Na). In NNO, Nb being lighter than Ta and of close ionic radius, all atoms contribute significantly to the eigendisplacements of the polar instability. The condensation of unstable modes is different depending on whether the transition atom is Ta or Nb in

FIG. 1. (Color online) Calculated phonon dispersion curves of cubic $NaNbO_3$ (a) and $NaTaO_3$ (b) at the GGA-PBEsol relaxed volume along the path $R-\Gamma-X-M-R$ of the cubic Brillouin zone. A color has been assigned to each point based on the contribution of each kind of atom to the associated dynamical matrix eigenvector (red for the Na atom, green for the Nb/Ta atom, and blue for O atoms). The Δ and T points of the Brillouin zone in NNO are not represented here.

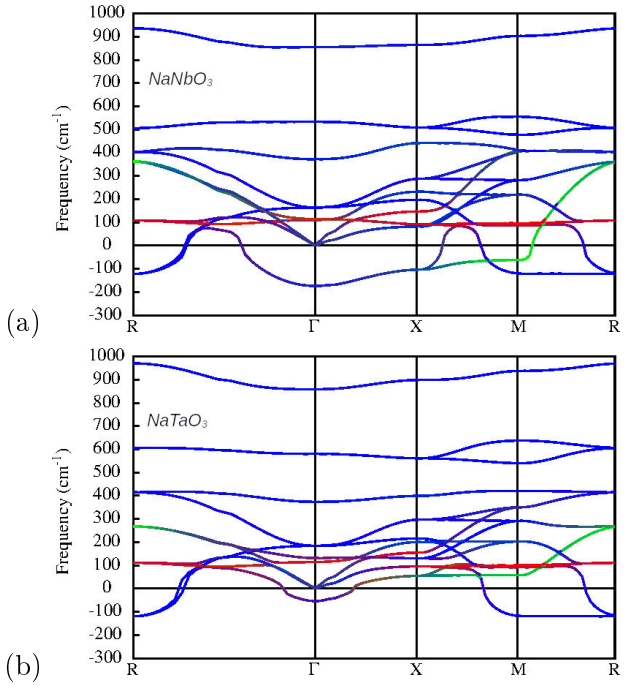

NaBO3 (B = Ta, Nb). For $NaTaO_3$, the condensation of the AFD modes stabilizes in the *Pnma* ground state all the other unstable modes observed in the high-symmetry phase. In NNO, however, as we shall see in the section V, it is rather the combined condensation of all these modes, at least two as in the $R\bar{3}c$ structure, that stabilizes the low energy structures. Before, let us first analyse the NNO phonons unstable modes separately.

IV. $NaNbO_3$ INSTABILITIES MODES ONE BY ONE

In this section, we successively analyze the condensations of different unstable modes observed in the phonon curves of the high-symmetry phase. The goal is to see how these modes condense when isolated and when combined, and thus to understand the importance of the couplings in the stabilization of this or that phase. Colored bars of Figures 2 and 3 visualize the energy gains relative to the high-symmetry cubic phase of different structures

TABLE II. Modes and soft phonon frequencies ω (cm^{-1}) of NNO and NTA high-symmetry at Γ, X, M, R, Δ and T points of the Brillouin zone. AP is the abbreviation of antipolar mode. The values in brackets are from Prosandeev[39].

k-points		Mode	Type	ω	
				$NaNbO_3$	$NaTaO_3$
Γ	$(0, 0, 0)$	Γ_4^-	FE	$174i$ ($121i$)	$54i$
Δ	$(0, \frac{1}{4}, 0)$	Δ_5	AP	$129i$	
X	$(\frac{1}{2}, 0, 0)$	X_5^-	AP	$103i$	
M	$(\frac{1}{2}, \frac{1}{2}, 0)$	M_3^+	AFD	$120i$ ($138i$)	$118i$
		M_3^-	AP	$62i$	
T	$(\frac{1}{2}, \frac{1}{2}, \frac{1}{4})$	T_4	AFD/AP	$121i$	
R	$(\frac{1}{2}, \frac{1}{2}, \frac{1}{2})$	R_4^+	AFD	$122i$ ($140i$)	$120i$

we have relaxed in NNO through the GGA-PBEsol and LDA approximations. In the GGA-PBEsol approximation, we performed two types of calculations: the GGA-PBEsol-1 (Fig. 2-left) calculation consisted in a total relaxation of the cell and the atomic positions and the GGA-PBEsol-2 (Fig. 3) calculation consisted in relaxing only the atomic positions but in a fixed cubic cell, i.e. by not allowing the strain.

Three zones indicated by curly brackets on the left can be analyzed from these graphs: the zone of the polar (FE) and antipolar electric (APE) distortions, the zone of the AFD distortion and the zone combining the FE/AFD and AFD/APE distortions. The last combined distortions will be discused in the Section V.

A. The polar and antipolar electric modes

Looking at the phonon dispersion curves of the cubic phase (Fig. 1), the unstable polar mode is the most significant (Γ_4^-, $174i\,cm^{-1}$) followed by the antipolar electric mode (Δ_5, $129i\,cm^{-1}$). In agreement with the previous study[21], our analysis of the eigendisplacements

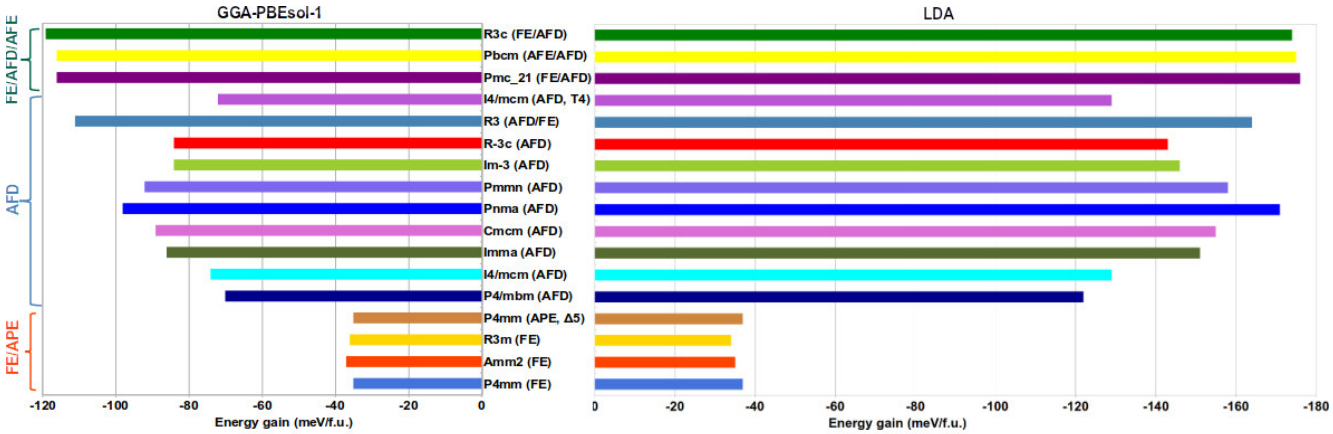

FIG. 2. (Color online) Energy gain (meV/f.u.) of different total relaxed structures in NNO calculated in GGA-PBEsol and LDA approximations. Magnitudes of the GGA-PBEsol tilts angles (°) are : $P4/mbm$ ($a^0a^0c^+$: $c^+ = 11.3/5.0^a$), $I4/mcm$ ($a^0a^0c^-$: $c^- = 11.9$), $Imma$ ($a^-a^-c^0$: $a^- = 9.0$), $Cmcm$ ($a^0b^-c^+$: $b^- = 8.7/4.7^a$, $c^+ = 9.0/6.1^a$), $Im\bar{3}$ ($a^+a^+a^+$: $a^+ = 7.0$), $R\bar{3}c$ ($a^-a^-a^-$: $a^- = 6.9$), $Pnmm$ ($a^-b^+b^+$: $a^- = 8.0$, $b^+ = 6.9$), $Pnma$ ($a^-b^+a^-$: $a^- = 8.5$, $b^+ = 9.4$). ^{a}: experimental value[47]. The zero of energy corresponds to the equilibrium cubic paraelectric $Pm\bar{3}m$ state.

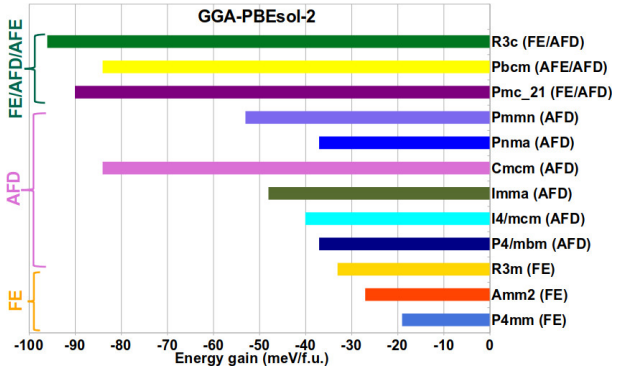

FIG. 3. (Color online) Energy gain (meV/f.u.) of different structures of NNO calculated by relaxing only the atomic positions but in a fixed cubic volume, i.e. by not allowing the strain (GGA-PBEsol-2).

corresponding to the Γ_4^- phonons shows that the B-Nb atoms are indeed involved in the motion in such a way that both atoms Na and Nb move out of phase with respect to the oxygen atoms (Table III), in contrast to what is observed in PZO polar unstable mode. Therefore, the Nb atom contributes significantly to the ferroelectric Γ_4^- mode in NNO. The mode effective charge associated to this unstable mode is $7.88e$, larger than in $NaTaO_3$ and

PZO.

TABLE III. Normalized real-space eigendisplacement for the unstable FE mode at Γ (z polarization) and associated TO mode effective charges (as defined in 32). The corresponding dynamical matrix eigenvector can be obtained by multiplying each value by the appropriate mass factor $\sqrt{M_{\text{ion}}}$.

Atom	$NaNbO_3$	$NaTaO_3$	$PbZrO_3$
Na	0.046	0.112	0.034
Nb/Ta/Zr	0.051	0.016	−0.014
$O_{\parallel}$	−0.107	−0.087	−0.067
$O_{\perp}$	−0.128	−0.130	−0.145
$\overline{Z}^*$	7.88	5.36	5.07

The $P4mm$ (royalblue bars, Fig. 2), $Amm2$ (orangered bars) and $R3m$ (gold bars) structure represent the condensations of the unstable polar modes along the directions [100], [110] and [111] respectively. The energy difference between the three structures is very small, about 1 meV/f.u. If NNO were only FE, according to the approximation used, the $Amm2$ structure would be the most stable FE GGA-PBEsol structure in this material ($Amm2$: −37 meV/f.u.; $R3m$: −36 meV/f.u. and $P4mm$: −35 meV/f.u.) with a spontaneous polarization equal to 49 μC/cm^2 and an indirect R−Γ gap of 2.1 eV. Our LDA calculations gives a different trend; it is rather the $P4mm$ structure which is the FE lowest energy ($P4mm$: −37 meV/f.u.; $Amm2$: −35 meV/f.u. and $R3m$: −34 meV/f.u.). Contrary to the intuition that one would have by observing the intensities of the instabilities in the phonon curves (Fig. 1), the condensation of the only FE unstable mode allows small energy gains. Concerning the APE unstable mode Δ_5, starting from the $Cmc2_1$ structure the system relaxes in $P4mm$ structure (Γ_4^-, peru bars) with the almost same total energy gain in both GGA-PBEsol and LDA (−35/−37 meV/f.u.). This result allows us to conclude that, unlike the Σ_2 APE mode in PZO[46], the Δ_5 APE mode in NNO cannot even condense itself.

B. The AFD modes

Among all instabilities, those caused by the rotations of oxygen octahedra, antiferrodistortive (AFD) modes, are the most common in perovskites[10–13]. Glazer's description are in terms of component tilts around the 'pseudo-cubic' axes, that is the cubic axes of the parent structure. The irrep (irreducible representation) associated with the inphase tilts is M_3^+ ($k = 1/2,\ 1/2,\ 0$) and that associated with the antiphase tilts is R_4^+ ($k = 1/2,\ 1/2,\ 1/2$)[13]. Both AFD modes are unstable in the high-symmetry cubic phase of NNO with significant intensities (M_3^+: $120i$ and R_4^+: $122i$) but, contrary to what has been observed in PZO[46], not higher but lower than polar FE and antipolar modes (Γ_4^-, $174i$ cm^{-1} and Δ_5, $129i$ cm^{-1}, respectively).

Now let us see how NNO would behave if it were only AFD. In the second zone of the Figure 2 (AFD distortion), we show the total relaxed energies of the AFD structures obtained by condensing the M_3^+ and R_4^+ modes, separated and combined. Whatever the approximation used, the hierarchy of AFD unstable modes stay the same. The lowest energy is achieved in the orthorhombic phase *Pnma* ($a^-b^+a^-$), combining two antiphase and one inphase rotations, as also found in PZO[46]. This phase is not observed in NNO, but it may allow us to understand why the coupling of its rotations with the polar FE orthorhombic displacements favors a significant energy gain to stabilize the $Pmc2_1$, a subgroup of *Pnma*. The AFD *P4/mbm* ($a = b = 5.4756/5.5639$[47], $c = 7.9066/7.8856$) and *Cmcm* ($a = 7.7195/7.7642$[47], $b = 7.8061/7.8550$, $c = 7.8109/7.8696$) phases were observed experimentally. On the one hand, from the results of our calculations, both AFD modes inphase M_3^+ and antiphase R_4^+ evolve almost in the same way when they are separately condensed in one, two or even three components. The structures $Im\bar{3}$ ($a^+a^+a^+$, yellowgreen bars) and $R\bar{3}c$ ($a^-a^-a^-$, red bars), condensing respectively the M_3^+ and R_4^+ modes in three components show the same energy gain (-84 meV/f.u., even if the LDA approximation slightly favors the $Im\bar{3}$ structure, -146 meV/f.u., more than the $R\bar{3}c$, -143 meV/f.u.), but their couplings with polar displacements favor the R_4^+ mode ($R3c$, $a_p^-a_p^-a_p^-$, $-119/-174$ meV/f.u., green bars) more than the M_3^+ mode ($R3$, $a_p^+a_p^+a_p^+$, $-111/-164$ meV/f.u., steelblue bars). On the other hand, we can notice that condensing M_3^+ and R_4^+ modes simultaneously (*Cmcm*, $a^0b^-c^+$, $-89/-155$ meV/f.u., orchid bars) is more favorable than condensing a single mode in two (*Imma*, $a^-a^-c^0$: $-86/-151$ meV/f.u., darkolivegreen bars) or three directions ($Im\bar{3}$

or $R\bar{3}c$). Moreover, coupling antiphase tilts in two directions and inphase tilt in the third direction (*Pnma*, $a^-b^+a^-$: −98/−171 meV/f.u., blue bars) is energetically more favorable than combining antiphase tilt in one direction and inphase tilts in two directions (*Pnmm*, $a^-b^+b^+$: −92/−158 meV/f.u., mediumslateblue bars).

Compared to the energy gain of the FE mode Γ_4^- (−37 meV/f.u.), we can see that the energy gain of the AFD modes M_3^+ and R_4^+, both separately and combined, are considerably larger (from 1.9 to 2.6 times lower for *P*4/*mbm* and *Pnma* respectively). This can explain why octahedral tilts corresponding to the M_3^+ and R_4^+ modes can be considered as primary order parameters, inducing the first two structural transitions, from the cubic into the T_2 and T_1 phases[21]. The AFD modes therefore play a crucial role in condensing the NNO ground state, as they select the AFE distortions, among competing structural variants, and at low temperature the rhombohedral *R*3*c* and the orthorhombic $Pmc2_1$ (both FE/AFD) symmetries which are energetically close to the orthorhombic AFE/AFD state *Pbcm*.

About the strain: Comparing the energy gains of GGA-PBEsol-1 and GGA-PBEsol-2 calculations, we notice that the strain relaxation plays a significant role in NNO, lowering the energy by 3 meV/f.u. in *R*3*m* and by 61 meV/f.u. in *Pnma*. It is the strain relaxation that allows to stabilize the *Amm*2 structure (from −27 to −37 meV/f.u.) further than the *R*3*m* (from −33 to −36) or the *Pnma* (from −37 to −98 meV/f.u.) further than the *Cmcm* (from −50 to −89 meV/f.u.) and *Pmmn* (from −53 to −92 meV/f.u.). It is also the strain relaxation that brings the *Pbcm* and $Pmc2_1$ structures at similar energies (from −86 to −116 meV/f.u. and from −90 to −116 meV/f.u. respectively). As for the *R*3*c* symmetry, it remains the most stable (from −96 to −119 meV/f.u.).

The discrepancies between the total energies of AFD and APE distortions is striking compared to what we observed in PZO[46], another AFE compound. While in PZO, the condensation of the Σ APE and S_4 AFD distortions converges to energies close to those obtained in *Imma* and *Pnma* structures (−215, −214, −169 and −224 meV respectively), the situation is totally different in NNO. Indeed, the condensation of the individual Δ_5 and T_4 distortions converges at total energies far higher than the *Imma*, *Cmcm* and *Pnma* structures (−16, −72, −86, −89 and −98 meV respectively). The coupling of modes is very crucial in this material to stabilize the low energy states FE/AFD and AFE/AFD and, as we have seen before, it is the unstable AFD modes that allow to lower the energies of the FE and APE modes.

V. TOWARDS THE LOWEST ENERGY STATE

Having explored the modes separately, we are now in a position to understand the combinations of modes that leads to lowest energy structures. As can be seen from Figure 2, and whatever the approximation used, we note that three structures converge at the lowest energies with close values: orthorhombic FE/AFD[110] $Pmc2_1$ (mauve bars), orthorhombic AFE/AFD $Pbcm$ (yellow bars) and rhombohedral FE/AFD[111] $R3c$ (green bars). The accurate energy gain (from the high-symmetry cubic reference $Pm\bar{3}m$ phase) of the three energetically ground states of NNO, from GGA-PBEsol and LDA approximations, are reported in Table IV.

TABLE IV. Energy gain (meV/f.u.), remanent instability (cm^{-1}), and total polarization P ($\mu C/cm^2$, Exp. 59 $\mu C/cm^2$ in $R3c$[48]) of the three low energy distortions in NNO optimized through GGA-PBEsol (GGAPBEs) and LDA approximations. The comparative values in brackets are taken from the reference[49]. The angle in the rhombohedral cell is 89.24° (Exp. 89.22°[50]). The condensed modes in $30i$ instability are relatively R_4^+ (1.45), T_4 (1.20) and Δ_5 (0.65).

Space	Energy gain		Instability		P
group	GGAPBEs	LDA	GGAPBEs	LDA	
Q: $Pmc2_1$	−116.1(−108.7)	−176.2	$0i$	$0i$	32(47)
P: $Pbcm$	−116.3(−106.3)	−175.0	$30i$	$0i$	
N: $R3c$	−119.2(−116.1)	−173.9	$0i$	$0i$	48(58)

According to the definition of AFE phase proposed by Rabe (Ref.[51]), we suggested in our earlier paper[46] that there must be, in addition, an alternative low energy FE phase obtained as a distortion of the same high symmetry reference, and application of an electric field must induce a first order transition AFE−FE phase producing a double hysteresis loop characteristic. The latter condition promotes a small energy difference and ease of transformation between the two phases. In fact, the key of an AFE phase is the nearest with the FE state and this is what we observe in the NNO.

Depending on the approximation used, our calculations lead to two different results on

the lowest energy state in NNO. When we consider the results obtained by the GGA-PBEsol approximation, it is the $R3c$ structure which constitutes the NNO lowest energy state, in agreement with experimental studies. Even keeping the cubic volume fixed (Fig. 3), i.e. not relaxing the strain, the low energy structure remains $R3c$ (-96 meV/f.u.) followed by $Pmc2_1$ (-90 meV/f.u.) and $Pbcm$ (-84 meV/f.u.). We can notice here again the importance of the strain in all these structures, making them gaining about 20 meV/f.u., much more in the $Pbcm$ (relative energy gain of 32 meV/f.u.) which stabilizes it at the same energy state as the $Pmc2_1$. But compared to the LDA approximation, the situation changes: it is now the $Pmc2_1$ structure wich is the lowest structure in energy. Even using the LDA Troullier-Martins pseudopotentials (LDA-TM), we get the same sequence: $Pmc2_1$ (-237.8 meV/f.u., curiously the same total energy gain as the relaxed $Pnma$), $Pbcm$ (-216.5 meV/f.u.) and $R3c$ (-196.9 meV/f.u.). This result allows us to conclude that when using the LDA approximation, NNO stabilizes in the AFD/FE orthorhombic phase ground state $Pmc2_1$, although in LDA-TM the total energy differences between the three phases are more significant. The last phase corresponds to the phase proposed experimentally[16,17] as the Q phase induced by applying an electric field to the $Pbcm$ phase at room temperature. If in LDA, the energy difference is of the order of 1 meV, in GGA-PBEsol on the other hand the two structures $Pmc2_1$ and $Pbcm$ converge at almost the same energy.

The $Pmc2_1$ phase has not been studied in the calculations made by Machado *et al.*[21], but, as far as the $Pbcm$ and $R3c$ phases are concerned, our results are in agreement with this study (LDA and GGA-WC). As for the phase sequence found in Ref.[49] ($N \rightarrow Q \rightarrow P$), our results differ with respect to the Q and P phases ($N \rightarrow P \rightarrow Q$). The LDA calculation, giving $Pmc2_1$ as the lowest energy phase, is not in agreement with the experimental[52] observations and may therefore mean that it is inappropriate to study this compound with this approximation. On the other hand, our GGA-PBEsol calculation is in agreement with the previous GGA-WC calculation, but seems to be more accurate, giving unambiguously $R3c$ as the lowest energy phase.

The non-centrosymmetric $R3c$ ($a^-_+a^-_+a^-_+$, $a^- = 7.1°$) phase combines the antiphase tilts (R^+_4 mode) and polar displacements (Γ^-_4 mode) of the Na, Nb, and O atoms along three cubic directions [111]. As for $Pbcm$ phase, it combines the $Imma$ (R^+_4) distortion with T_4 (complex AFD) and Δ_5 (APE). Finally, the $Pmc2_1$ phase, defined as a subgroup of the $Pnma$ phase, shows an unusual distortion; condensing complex rotations on alternative

layers $a^-a^-b^+/a^-a^-b^-$ ($a^- = 6.8°$, $b^+ = 8.3°$ and $b^- = 6.9°$) as in *Pbcm*, but while the *Pbcm* phase favors APE motion in the orthorhombic *ab*-plane, i.e. in the cubic direction [100], the $Pmc2_1$ phase is polar along the orthorhombic *b*-axis, i.e. in the cubic plane [110]. All these structural similarities between the last two phases[49] and the small difference in energy between them allow us to argue that, at room temperature, AFE-*Pbcm* phase of NNO should transforms into FE-$Pmc2_1$ phase upon application of an electric field.

The low energy structure $Pmc2_1$ results mainly from the high stability of the *Pnma* phase. The calculated spontaneous polarization of NNO for the FE/AFD $Pmc2_1$ and $R3c$ structures given in Table IV are found to be 32 μC/cm^2 and 48 μC/cm^2 respectively, which are comparable to that we obtained for the conventional ferroelectric rhombohedral $KNbO_3$ (41 μC/cm^2) and $BaTiO_3$ (42 μC/cm^2), but significantly smaller than for tetragonal $PbTiO_3$ (97 μC/cm^2).

Concerning the $Pmc2_1$ structure, we have relaxed the two other subgroups of the *Pnma* phase, namely: $Pna2_1$ and $Pnm2_1$[20]. The last two structures converge to the same total energy which is higher than the total relaxed energy of the $Pmc2_1$ (GGA-PBEsol: $-111/-116$ and LDA: $Pnm2_1 = -174/Pna2_1 = -175/-176$ meV/f.u. respectively). This result allows us to state that, of the three subgroups of the *Pnma* distortion, the $Pna2_1$ and $Pnm2_1$ distortions are unlikely in NNO in favor of the more stable $Pmc2_1$ structure. Concerning the $30i$ instability observed in the *Pbcm* phase, its condensation gives the $Pca2_1$ structure. When we condense this last structure, according to what was found in Ref.[22], its total energy remains at the same level as the *Pbcm* using LDA approximation (-175.0 meV/f.u.), but slightly lower in energy for GGA-PBEsol calculation ($-116.4/-116.3$ meV/f.u. $\Rightarrow -0.1$ meV/f.u.). The small energy difference between these three structures (N, P, Q), whatever the approximation used, could explain the coexisting ferroelectric and antiferroelectric structures observed in experiments[48], and thus it is obviously the key characteristic of antiferroelectricity[46,51].

To go further, let us now analyze the details concerning the three phases that are the subject of our discussion in this section. What are the main and secondary modes that condense in each of these phases and what are their relative contributions? Figures 4 reports the modes that condense in the $Pmc2_1$ and *Pbcm* (some authors use the alternative arrangement *Pbma*) phases.

Concerning the main modes, whatever the approximation used, we notice that on the one hand the hierarchy of amplitudes is in agreement with the experimental results, and

FIG. 4. (Color online) Relative contributions of phonon modes, analyzed with AMPLIMODES, in the $Pmc2_1$ (a) and $Pbcm$ (b) phases of NNO relaxed in GGA-PBEsol (green columns) and LDA (red columns) compared to the experimental data (blue columns, Ref.[53]). The main modes consist of either oxygen octahedra rotation (R_4^+, M_3^+ and T_4) or polar/antipolar displacements (Γ_4^-/Δ_5), while the additional modes consist of couplings with cations (M_5^-, R_5^+, X_3^- and X_5^+) or oxygen displacements (Γ_5^-, T_2 and M_2^+). The $R3c$ condense two main modes: $R_4^+(0.89/0.93^{48})$ and $\Gamma_4^-(0.42/0.42)$.

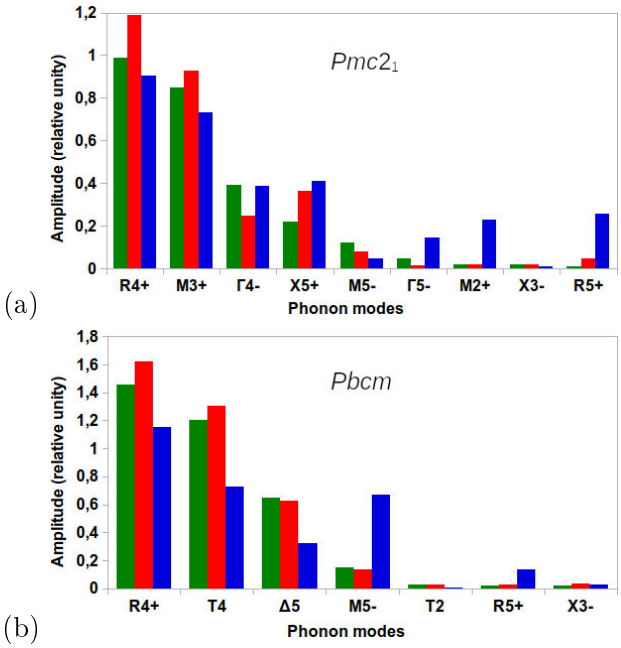

on the other hand it is the AFD R_4^+ mode which contributes most to the stabilization of these three phases. However, significant differences from experimental values are observed for some secondary modes that condense in the $Pbcm$ (M_5^-) and $Pmc2_1$ (X_5^+, Γ_5^-, M_2^+ and R_5^+). Given that the Δ_5 mode, according to our calculations, cannot even condense itself, we can highlight that in NNO, the AFD R_4^+ mode is very preponderant in the coupling with the Δ_5 mode and thus gives rise to the $Pbcm$ phase.

It is instructive to compare the relative contribution of each atom to the distortion associated with each irrep (Fig. 5). The colored columns of Figure 5 allow us to observe that, in NNO, on the one hand the AFD displacements of the oxygens (R_4^+ and M_3^+) are favored over the ferrodistortive displacements (Γ_5^-, M_2^+ and T_2), on the other hand, the contributions of the atoms are significant and with close intensities in both Γ_4^- polar and Δ_5, M_5^- antipolar modes. This last observation allows us to argue that the coexistence of low energy phases

FIG. 5. (Color online) Atomic contributions by mode in the $Pmc2_1$ and $Pbcm$ phases of NNO. The atomic contributions of Na, Nb and O atoms in the Γ_4^- mode of $Pmc2_1$ are very close (Na: 0.58, Nb: 0.51, O1: -0.57 and O2: -0.29), while in the same mode for $R3c$, it is the Na atom wich contributes significantly (Na: 0.72, Nb: 0.32, O1: -0.27 and O2: -0.55).

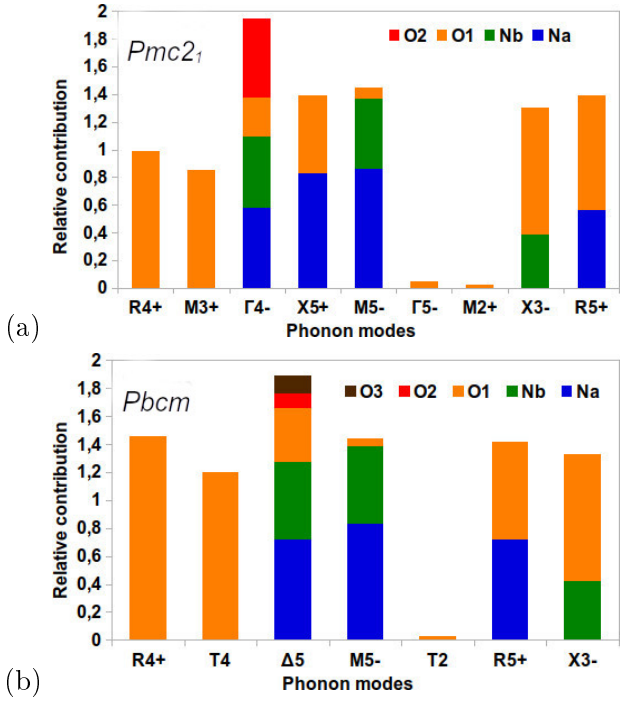

is probably related to the simultaneous structural distortion caused by the displacement of Na and Nb ions from their equilibrium positions.

Let us finally present in the Table V how the amplitudes of the modes evolve in the different structures. Interestingly, we can note here that the amplitude of the modes remains the same or increases when they are coupled. This result allows us to argue that the coupling of modes is very favored to stabilize the phases of the lowest energies in NNO. Although they appear as unstable modes in the high-symmetry phase, the X_5^- $(103i)$ and M_3^- $(62i)$ APE modes do not contribute to the stabilization of any of the observed NNO structures. The simultaneous condensation of two (in $R3c$) or three (in $Pmc2_1$ or $Pbcm/Pca2_1$) of the five main modes as reported in figures 4 is sufficient to stabilize them. Comparing the pseudocubic volumes of the different structures, we reach the same conclusion as in the PZO[46]; FE and AFE instabilities tend to increase the volume while AFD ones reduce them.

Table VI reports the NNO relaxed positions in the three low energy structures $Pmc2_1$, $Pbcm$ and $R3c$, respectively. We can note here again the agreement of our optimized values

TABLE V. Evolution of the pseudocubic volume (Å^3) and amplitudes of the modes in the main structures of NNO.

Symmetry	V	Γ_4^-	Δ_5	R_4^+	T_4	M_3^+
$Pm\bar{3}m$	61.29	$174i$	$129i$	$122i$	$121i$	$120i$
$Amm2$	61.80	0.29				
$P4mbm$	59.26					0.82
$Cmcm$	58.84			0.89		0.92
$Pmmn$	58.80			1.16		1.41
$Pnma$	58.56			1.07		0.82
$Pmc2_1$	59.22	0.39		0.99		0.85
$Pbcm$	59.09		0.65	1.45	1.20	
$R3c$	59.60	0.42		0.89		

compared to the previous experimental results.

VI. CONCLUSIONS

In this study, we have conducted a systematic investigation of energy lowering and ways of coupling in $NaNbO_3$ through different phases, observed and unobserved experimentally. The sodium niobate is an insulator with an indirect gap of 1.65 eV between R and Γ points of the Brillouin zone. The phonon dispersion curves from the high-symmetry cubic perovskite phase have been reported to have many unstable branches. The richness of the phonon curves and the multitude of phase transitions of $NaNbO_3$ are the subject of several studies both experimental and theoretical. By condensing the unstable modes one by one, we found that no single condensed mode corresponds to the ground state in this material. Instead, it is the combination of several modes, thanks to their coupling, that brings $NaNbO_3$ to it's lowest energy states. Our calculations reveal that, whatever the approximation used, both the antiferroelectric and ferroelectric distortions in $NaNbO_3$ yield close lowering of the energy

TABLE VI. Cell parameters (Å) and atomic positions of NNO in the orthorhombic $Pmc2_1$, orthorhombic $Pbcm$, and hexagonal $R3c$ phases, respectively, in comparison with experimental data.

Q		$Pmc2_1$			Ref.[53]	
a		7.7421			7.7633	
b		5.5024			5.5143	
c		5.5608			5.5655	
Site	x	y	z	x	y	z
Na (2a)	0.0000	0.2599	0.0483	0.0000	0.2500	0.7820
Na (2b)	0.5000	0.2588	0.0806	0.5000	0.2510	0.8520
Nb (4c)	0.7495	0.7556	0.0620	0.7500	0.7540	0.8080
O1 (2a)	0.0000	0.6887	0.0377	0.0000	0.1750	0.2630
O2 (2b)	0.5000	0.8132	0.0160	0.5000	0.3220	0.2850
O3 (4c)	0.7175	0.5385	0.3205	0.2300	0.5500	0.0580
O4 (4c)	0.7809	0.0395	0.2462	0.2710	0.9640	0.5130
P		$Pbcm$			Ref.[53]	
a		5.4945			5.5327	
b		5.5602			5.5630	
c		15.4732			15.6450	
Site	x	y	z	x	y	z
Na1 (4c)	0.7431	0.2500	0.0000	0.2100	0.7500	0.0000
Na2 (4d)	0.2591	0.7080	0.2500	0.2120	0.7570	0.2500
Nb (8e)	0.2447	0.2270	0.1252	0.2497	0.2500	0.1250
O1 (4c)	0.3139	0.2500	0.0000	0.3260	0.2500	0.0000
O2 (4d)	0.1850	0.2723	0.2500	0.2090	0.2310	0.2500
O3 (8e)	0.4614	-0.0323	0.1418	0.5180	0.0140	0.1370

as compared to the higher energy cubic paraelectric phase : rhombohedral FE/AFD $R3c$, orthorhombic FE/AFD $Pbcm$, and orthorhombic FE/AFD $Pmc2_1$. These phase transitions are mainly driven by zone boundary phonon instabilities at R and M points and along the line T (connecting the M and R points). The GGA-PBEsol approach gives: *1)* a $Pbcm$ and $R3c$ phase hierarchy in agreement with both experimental and theoretical data (-116 and -119 meV/f.u. respectively), stabilizing this material in the $R3c$ phase as the ground state; *2)* the $Pbcm$ and $Pmc2_1$ phases relax at almost the same total energy (-116 meV/f.u.). In contrast, our LDA calculations yields a different tendency, stabilizing the orthorhombic FE/AFD phase $Pmc2_1$ in the ground state, followed by the $Pbcm$ phase then the $R3c$ (-176, -175 and -174 meV/f.u. respectively). This set of results allows us to suggest that the GGA-PBEsol calculations are a reliable approach to study the structural and dynamical complexity of the perovskite compound $NaNbO_3$. In both calculations we find small energy difference between the three phases, of the order of 3 meV/f.u. for GGA-PBEsol and 1 meV/f.u. for LDA, which is a key characteristic of antiferroelectricity. In any case, the close proximity of energy between the two phases $Pbcm$ and $Pmc2_1$ allows us to state that the application of an electric field could bring the the AFE/AFD-$Pbcm$ phase towards the FE/AFD $Pmc2_1$ phase rather than towards the FE/AFD $R3c$.

CONFLICTS OF INTEREST

The authors declare no competing financial interest.

ACKNOWLEDGMENTS

This work has been supported by the PRD-CCD ARES 2019-2024 project: *Le coltan du Kivu: Capacité de traitement physico-chimique et études d'applications.* Calculations were carried out used the facilities provided by the CECI supercomputing center[54] thanks to the Université de Liège/Belgium.

---

[1] Z. Liu, T. Lu , J. Ye , G. Wang , X. Dong , R. Withers , Y. Liu, Adv. Mater. Technol. **3 (9)**, 1800111 (2018). https://doi.org/10.1002/admt.201800111

[2] N. Novak, F. Weyland, S. Patel, H. Guo, X. Tan, J. Rödel, J. Koruza, Phys. Rev. B **97**, 094113 (2018). https://doi.org/10.1103/PhysRevB.97.094113

[3] M. M. Vopson, G. Caruntu and X. Tan, Scr. Mater. **128**, 61 (2017). https://doi.org/10.1016/j.scriptamat.2016.10.004

[4] G. Shirane, R. Newnham, and R. Pepinsky, Phys. Rev. **96**, 581 (1954). https://doi.org/10.1103/PhysRev.96.581

[5] S. Lanfredi, M. H. Lente, and J. A. Eiras, Appl. Phys. Lett. **80**, 2731 (2002). https://doi.org/10.1063/1.1470260

[6] B. Yang, J. Bian, L. Wang, J. Wang, Y. Du, Z. Wang, C. Wu and Y. Yang, Phys. Chem. Chem. Phys., **21**, 11697-11704 (2019). https://doi.org/10.1039/C9CP01763A

[7] J. H. Jung, M. Lee, J.-I. Hong, Y. Ding, C.-Y. Chen, L.-J. Chou, and Z. L. Wang, ACS Nano **5**, 10041 (2011). https://doi.org/10.1021/nn2039033

[8] Y. Saito, H. Takao, T. Tani, T. Nonoyama, K. Takatori, T. Homma, T. Nagaya, and M. Nakamura, Nature London **432**, 84 (2004). http://dx.doi.org/10.1038/nature03028

[9] J.-F. Li, K. Wang, B.-P. Zhang, and L.-M. Zhang, J. Am. Ceram. Soc. **89**, 706 (2006). https://doi.org/10.1111/j.1551-2916.2005.00743.x

[10] A. M. Glazer, Acta Cryst. B **28**, 3384 (1972). https://doi.org/10.1107/S0567740872007976

[11] A. M. Glazer, Acta Cryst. A **31**, 756 (1975). https://doi.org/10.1107/S0567739475001635

[12] P. M. Woodward, Acta Cryst. B **53**, 44 (1977). https://doi.org/10.1107/S0108768196012050

[13] C. Howard and H. Stokes, Acta Cryst. B **54**, 782 (1998). https://doi.org/10.1107/S0108768198004200

[14] B. T. Matthias, Phys. Rev. **75**, 1771 (1949). https://doi.org/10.1103/PhysRev.75.1771

[15] H. D. Megaw, Ferroelectrics **7**, 87 (1974). https://doi.org/10.1080/00150197408237956

[16] V. A. Shuvaeva, M. Y. Antipin, S. V. Lindeman, O. E. Fesenko, V. G. Smotrakov, and Y. T. Struchkov, Ferroelectrics **141**, 307 (1993). https://doi.org/10.1080/00150199308223458

[17] R. A. Shakhovoy, S. I. Raevskaya, L. A. Shakhovaya, D. V. Suzdalev, I. P. Raevski, Yu. I. Yuzyuk, A. F. Semenchev and M. El Marssi, J. Raman Spectrosc. **43**, 1141 (2012). https://doi.org/10.1002/jrs.3140

[18] M. D. Peel, S. P. Thompson, A. Daoud-Aladine, S. E. Ashbrook, and P. Lightfoot, Inorg. Chem. **51**, 6876 (2012). https://doi.org/10.1021/ic3006585

[19] Y. Shiratori, A. Magrez, W. Fischer, C. Pithan, and R. Waser, J. Phys. Chem. C **111**, 18493 (2007). https://doi.org/10.1021/jp0738053

[20] K. E. Johnston, C. C. Tang, J. E. Parker, K. S. Knight, P. Lightfoot, and S. E. Ashbrook, J. Am. Chem. Soc. **132**, 8732 (2010). https://doi.org/10.1021/ja101860r

[21] R. Machado, M. Sepliarsky, and M. G. Stachiotti, Phys. Rev. B **84**, 134107 (2011). https://doi.org/10.1103/PhysRevB.84.134107

[22] Y. Yang, B. Xu, C. Xu, W. Ren, and L. Bellaiche, Phys. Rev. B **97**, 174106 (2018). https://doi.org/10.1103/PhysRevB.97.174106

[23] X. Gonze, F. Jollet, F. Abreu Araujo, D. Adams, B. Amadon, T. Applencourt, C. Audouze, J.-M. Beuken, J. Bieder, A. Bokhanchuk, E. Bousquet, F. Bruneval, D. Caliste, M. Cote, F. Dahm, F.Da Pieve, M. Delaveau, M. Di Gennaro, B. Dorado, C. Espejo, G. Geneste, L. Genovese, A. Gerossier, M. Giantomassi, Y. Gillet, D.R. Hamann, L. He, G. Jomard, J. Laflamme Janssen, S. Le Roux, A. Levitt, A. Lherbier, F. Liu, I. Lukacevic, A. Martin, C. Martins, M.J.T. Oliveira, S. Ponce, Y. Pouillon, T. Rangel, G.-M. Rignanese, A.H. Romero, B. Rousseau, O. Rubel, A.A. Shukri, M. Stankovski, M. Torrent, M.J. Van Setten, B. Van Troeye, M.J. Verstraete, D. Waroquier, J. Wiktor, B. Xu, A. Zhou, J.W. Zwanziger, Computer Phys. Comm. **205**, 106 (2016). https://www.abinit.org/sites/default/files/ABINIT16.pdf

[24] X. Gonze, B. Amadon, G. Antonius, F. Arnardi, L. Baguet, J.-M. Beuken, J. Bieder, F. Bottin, J. Bouchet, E. Bousquet, N. Brouwer, F. Bruneval, G. Brunin, T. Cavignac, J.-B. Charraud, Wei Chen, M. Cote, S. Cottenier, J. Denier, G. Geneste, Ph. Ghosez, M. Giantomassi, Y. Gillet, O. Gingras, D.R. Hamann, G. Hautier, Xu He, N. Helbig, N. Holzwarth, Y. Jia, F. Jollet, W. Lafargue-Dit-Hauret, K. Lejaeghere, M.A.L. Marques, A. Martin, C. Martins, H.P.C. Miranda, F. Naccarato, K. Persson, G. Petretto, V. Planes, Y. Pouillon, S. Prokhorenko, F. Ricci, G.-M. Rignanese, A.H. Romero, M.M. Schmitt, M. Torrent, M.J. van Setten, B. Van Troeye, M.J. Verstraete, G. Zerah and J.W. Zwanzig, Computer Phys. Comm. **248**, 107042 (2020). https://doi.org/10.1016/j.cpc.2019.107042

[25] http://www.abinit.org

[26] M. A. L. Marques, M. J. T. Oliveira, T. Burnus, Computer Phys. Comm. **183**, 2272 (2012). https://doi.org/10.1016/j.cpc.2012.05.007

[27] D. R. Hamann, Phys. Rev. B **88**, 085117 (2013). https://doi.org/10.1103/PhysRevB.88.085117

[28] M. J. van Setten, M. Giantomassi, E. Bousquet, M. J. Verstraete, D. R. Hamann, X. Gonze, G.-M. Rignanese, Computer Physics Communications **226**, 39-54 (2018). https://doi.org/10.1016/j.cpc.2018.01.012

[29] http://www.pseudo-dojo.org/index.html

[30] J. P. Perdew, A. Ruzsinszky, G. I. Csonka, O. Vydrov, G. Scuseria, L. Constantin, X. Zhou and K. Burke, Phys. Rev. Lett. **100**, 136406 (2008). https://doi.org/10.1103/PhysRevLett.100.136406

[31] J. P. Perdew and Y. Wang, Phys. Rev. B **45**, 13244 (1992). https://doi.org/10.1103/PhysRevB.45.13244

[32] X. Gonze and C. Lee, Phys. Rev. B **55**, 10355 (1997). https://doi.org/10.1103/PhysRevB.55.10355

[33] R. D. King-Smith, D. Vanderbilt, Phys. Rev. B **47**, 1651-1654 (1993). https://doi.org/10.1103/physrevb.47.1651

[34] H. T. Stokes and D. M. Hatch, J. Appl. Cryst. **38**, 237-238 (2005). http://stokes.byu.edu/iso/findsym.php

[35] H. T. Stokes, D. M. Hatch, B. J. Campbell, ISOTROPY; Brigham Young University: Provo, Utah, (2007). http://stokes.byu.edu/isotropy.html.

[36] D. Orobengoa, C. Capillas, M.I. Aroyo, and J.M. Perez-Mato, J. Appl. Cryst. **A42**, 820-833 (2009). http://www.cryst.ehu.es/cryst/amplimodes.html.

[37] B. J. Campbell, H. T. Stokes, D. E. Tanner, and D. M. Hatch, J. Appl. Cryst. **39**, 607 (2006). http://stokes.byu.edu/iso/isodistort.php.

[38] H. Kato, H. Kobayashi, and A. Kudo, J. Phys. Chem. B **106**, 12441 (2002). https://doi.org/10.1021/jp025974n

[39] S. A. Prosandeev, Phys. Stat. Sol. B **47**, No. 11, 2130-2134 (2005). https://doi.org/10.1134/1.2131156

[40] R. Oja and R. M. Nieminem, Phys. Rev. B **80**, 205420 (2009). https://doi.org/10.1103/PhysRevB.80.205420

[41] W. Zhong, R. D. King-Smith, and D. Vanderbilt, Phys. Rev. Lett. **72**, 3618 (1994). https://doi.org/10.1103/PhysRevLett.72.3618

[42] Ph. Ghosez, J.-P. Michenaud, and X. Gonze, Phys. Rev. B **58**, 6224 (1998). https://doi.org/10.1103/PhysRevB.58.6224

[43] S. E. Ashbrook, L. Le Polles, R. Gautier, C. I. Pickard and R. I. Walton, Phys. Chem. Chem. Phys. **8**, 3423-3431 (2006). https://doi.org/10.1039/B604520K

[44] P. Borlido, J. Schmidt, A. W. Huran, F Tran, M. A. L. Marques, and S. Botti, npj Comput Mater **6**, 96 (2020). https://doi.org/10.1038/s41524-020-00360-0

[45] D.I. Bilc, R. Orlando, R. Shaltaf, G.-M. Rignanese, J. Iniguez and Ph. Ghosez, Phys. Rev. B**77**, 165107(2008). http://dx.doi.org/10.1103/PhysRevB.77.165107

[46] S. Amisi, Eur. Phys. J. Plus **136**, 653 (2021). https://doi.org/10.1140/epjp/s13360-021-01639-x

[47] C. N. W. Darlington and K. S. Knight, Acta Cryst. B **55**, 24 (1999). https://doi.org/10.1107/S010876819800963X

[48] S. K. Mishra, N. Choudhury, S. L. Chaplot, P. S. R. Krishna, R. Mittal, Phys. Rev. B **76**, 024110 (2007). https://doi.org/10.1103/PhysRevB.76.024110

[49] H. Shimizu, H. Guo, S.E. Reyes-Lillo, Y. Mizuno, K.M. Rabe, C.A. Randall, Dalton Trans. **44** (23), 10763–10772 (2015). https://doi.org/10.1039/C4DT03919J

[50] C. N. W. Darlington and H. D. Megaw, Acta Cryst. B**29**, 2171 (1973). https://doi.org/10.1107/S0567740873006308

[51] K. M. Rabe, *Antiferroelectricity in Oxides: a reexamination*, Functional Metal Oxides: New Science and Novel Applications, edited by S. Ogale and V. Venkateshan, Wiley, New York, 2012.

[52] T. Arioka, H. Taniguchi, M. Itoh, K. Oka, R. Wang and D. Fu, Ferroelectrics **401**, 51 (2010) https://doi.org/10.1080/00150191003670408

[53] J. Koruza, J. Tellier, B. Malič , V. Bobnar, and M. Kosec, J. Appl. Phys. **108**, 113509 (2010). https://doi.org/10.1063/1.3512980

[54] https://www.ulg.ac.be/cms/c$_$3826073/fr/nic4, http://www.ceci-hpc.be/